

# Piezoelectricity in Monolayer Hexagonal Boron Nitride

Pablo Ares, Tommaso Cea, Matthew Holwill, Yi Bo Wang, Rafael Roldán, Francisco Guinea,\*  
Daria V. Andreeva, Laura Fumagalli,\* Konstantin S. Novoselov,\* and Colin R. Woods

2D hexagonal boron nitride (hBN) is a wide-bandgap van der Waals crystal with a unique combination of properties, including exceptional strength, large oxidation resistance at high temperatures, and optical functionalities. Furthermore, in recent years hBN crystals have become the material of choice for encapsulating other 2D crystals in a variety of technological applications, from optoelectronic and tunneling devices to composites. Monolayer hBN, which has no center of symmetry, is predicted to exhibit piezoelectric properties, yet experimental evidence is lacking. Here, by using electrostatic force microscopy, this effect is observed as a strain-induced change in the local electric field around bubbles and creases, in agreement with theoretical calculations. No piezoelectricity is found in bilayer and bulk hBN, where the center of symmetry is restored. These results add piezoelectricity to the known properties of monolayer hBN, which makes it a desirable candidate for novel electromechanical and stretchable optoelectronic devices, and pave a way to control the local electric field and carrier concentration in van der Waals heterostructures via strain. The experimental approach used here also shows a way to investigate the piezoelectric properties of other materials on the nanoscale by using electrostatic scanning probe techniques.

Piezoelectricity is an important property of noncentrosymmetric crystals that allows conversion of mechanical strain into electric field, and vice versa.<sup>[1]</sup> Recently, 2D crystals have shown to be a unique platform to investigate and exploit such property for many reasons. First, they have the ability to sustain large strain (up to 10%) before rupture or plastic deformation,<sup>[2]</sup> while this is challenging to achieve in 3D crystals. Second, many crystals are found to be piezoelectric only when reduced to two-dimensionality. This is the case of semiconducting


transition metal dichalcogenides, in which inversion symmetry is broken only in their 2D forms, as recently observed in single-layer MoS<sub>2</sub>.<sup>[3]</sup> Furthermore, 2D crystals are likely to show areas of nonuniform strain near corrugations or bubbles that naturally form on substrates.<sup>[4]</sup> In such areas, strained-induced local charge densities,  $\rho$ , are expected to appear owing to the local variation in polarization,  $\mathbf{P}$ , since  $\rho(r) = -\nabla \cdot \mathbf{P}(r)$ .<sup>[5]</sup>

2D hexagonal boron nitride (hBN) is a van der Waals crystal with remarkable properties<sup>[2a,6]</sup> and is an essential component of many new 2D technologies.<sup>[7]</sup> Recently, single-layer hBN has been theoretically predicted to be piezoelectric due to its broken inversion symmetry.<sup>[5,8]</sup> Boron and nitrogen atoms in hBN are arranged in a honeycomb lattice similarly as graphene, but the presence of different elements in the two sublattices of its unit cell makes it noncentrosymmetric.

On the other hand, its bilayer and bulk counterparts recover the inversion symmetry and, therefore, no piezoelectricity is expected.<sup>[5,8]</sup> Here, we report experimental evidence of piezoelectricity in monolayer hBN by directly visualizing the strained-induced electric field in hBN single layers using electrostatic force microscopy (EFM).<sup>[9]</sup> EFM images of monolayer hBN show enhanced electric contrast in correspondence of nonhomogenous strain areas around bubbles and creases. Such contrast vanishes on bilayer and few-layer hBN, as expected. We support our experimental findings with

Dr. P. Ares, Dr. M. Holwill, Dr. Y. B. Wang, Dr. L. Fumagalli,  
Prof. K. S. Novoselov, Dr. C. R. Woods  
Department of Physics & Astronomy and National Graphene Institute  
University of Manchester  
Manchester M13 9PL, UK  
E-mail: laura.fumagalli@manchester.ac.uk;  
Konstantin.Novoselov@manchester.ac.uk

Dr. T. Cea, Prof. F. Guinea  
Imdea Nanociencia  
Faraday 9, Madrid 28049, Spain  
E-mail: francisco.guinea@manchester.ac.uk

 The ORCID identification number(s) for the author(s) of this article can be found under <https://doi.org/10.1002/adma.201905504>.

© 2019 The Authors. Published by WILEY-VCH Verlag GmbH & Co. KGaA, Weinheim. This is an open access article under the terms of the Creative Commons Attribution License, which permits use, distribution and reproduction in any medium, provided the original work is properly cited.

DOI: 10.1002/adma.201905504

Dr. R. Roldán  
Instituto de Ciencia de Materiales de Madrid  
Sor Juana Inés de la Cruz 3, Madrid 28049, Spain  
Prof. F. Guinea  
Department of Physics & Astronomy  
University of Manchester  
Manchester M13 9PL, UK

Dr. D. V. Andreeva  
Department of Materials Science and Engineering  
National University of Singapore  
Singapore 117575, Singapore

Prof. K. S. Novoselov  
Centre for Advanced 2D Materials  
National University of Singapore  
Singapore 117546, Singapore

Prof. K. S. Novoselov  
Chongqing 2D Materials Institute  
Liangjiang New Area  
Chongqing 400714, China

detailed theoretical simulations, solving the elasticity equations in a honeycomb lattice for deformations that mimic the observed bubbles and creases.

EFM is a noncontact scanning probe technique that maps the local electrostatic interaction between the tip and the sample under study.<sup>[9]</sup> We acquired EFM images by applying an AC voltage bias at frequency  $\omega$  to the tip and measured the frequency shift of the cantilever at its mechanical resonance, detecting the electric response at the first and second harmonics,  $\omega$  and  $2\omega$ , respectively.<sup>[10]</sup> We thus obtained two simultaneous EFM images: the electric image at  $\omega$ , which is proportional to the electric field on the surface,<sup>[10a,c,11]</sup> and the dielectric image at  $2\omega$ , which depends only on the tip-sample capacitive interaction and the dielectric properties of the sample<sup>[10a,b]</sup> (see the Experimental Section and Section S1 of the Supporting Information). The latter was required here to investigate the impact of local capacitive variations on the electric image.

We applied EFM to monolayer, bilayer, and few-layer hBN resting on top of either thick hBN crystals (thickness  $\approx 5$ – $15$  nm) or graphene on SiO<sub>2</sub>/Si substrates, and not directly on top of SiO<sub>2</sub>/Si substrates. This is because the use of a 2D crystal as bottom layer promotes the formation of nonuniform strain areas in the top layer. Such areas are observed around bubbles and creases filled with hydrocarbons that spontaneously appear in van der Waals heterostructures.<sup>[4]</sup> Furthermore, the use of thick hBN and graphene as bottom layers is beneficial to avoid the influence of localized charges trapped at the SiO<sub>2</sub> interface, facilitating the visualization of strained-induced electric fields in the monolayer hBN. We fabricated monolayer-hBN/thick-hBN and

monolayer-hBN/graphene heterostructures using the standard dry transfer technique<sup>[12]</sup> (see the Experimental Section).

Figure 1 focuses on the results obtained for monolayer hBN on top of thick hBN crystals. Figure 1a is a representative topography image of a monolayer hBN region with several bubbles and creases. The corresponding EFM electric image (Figure 1b) shows high contrast over the bubbles which is mainly due to the presence of molecules inside the bubbles. However, it also shows high contrast around the bubbles where the substrate is flat, extending hundreds of nanometers and connecting various bubbles. A different behavior is found in the corresponding dielectric image (see Figure S2c in the Supporting Information). This shows the characteristic enhanced contrast over the bubbles caused by the material trapped inside,<sup>[10b]</sup> but no contrast around or between them. The absence of dielectric contrast outside the bubbles rules out that the origin of the electric contrast in these regions is a local change in dielectric properties. In particular, this allows discarding that the electric contrast outside the bubbles is caused by molecules that might be trapped below the monolayer. Electric and dielectric images obtained in other regions confirm these observations (see Figure S2d–f in the Supporting Information). Furthermore, we did not observe such bright areas in flat regions of the monolayer in the absence of bubbles and creases (see Figure S3 in the Supporting Information). This again implies that the electric field variations detected around them do not originate from molecules trapped at the hBN/hBN or hBN/SiO<sub>2</sub> interface. Close-up images confirmed these observations. Figure 1c shows the topography image of a triangular bubble. The regions in the immediate vicinity of

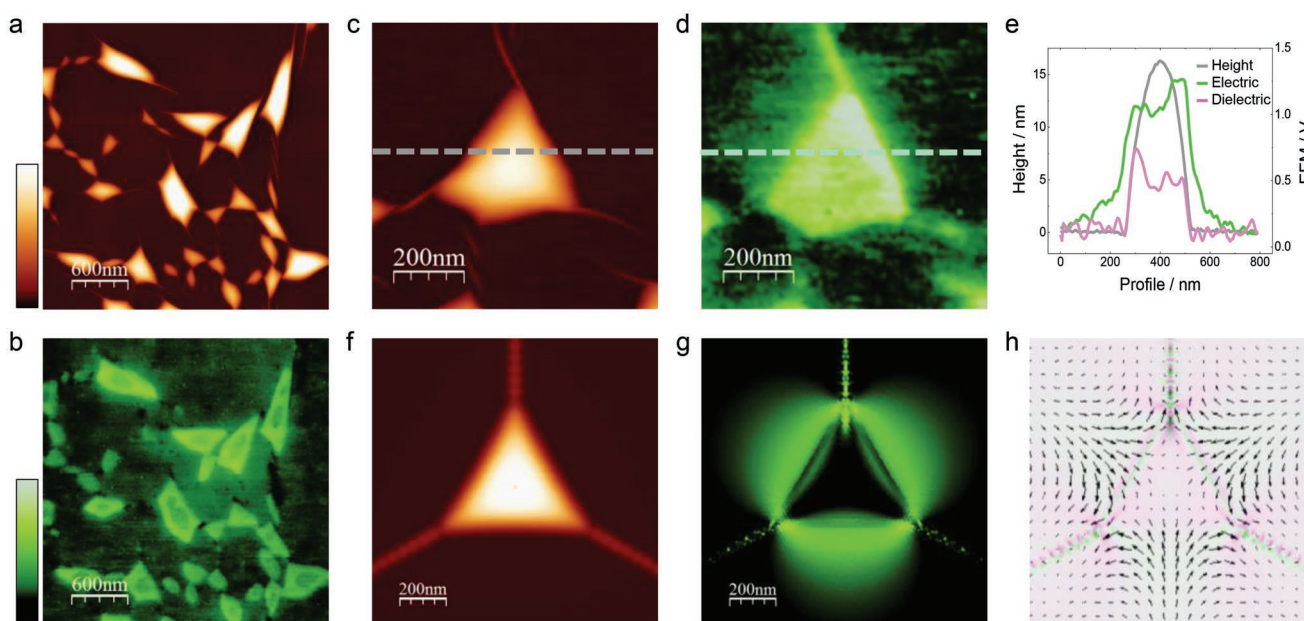


**Figure 1.** Monolayer hBN on thick hBN crystals. a) Topography of a representative region with bubbles and creases. b) Corresponding EFM electric image, showing enhanced contrast around and between bubbles. c) Topography and d) electric images of a triangular bubble. e) Profiles along the lines in (c) and (d) and in the corresponding dielectric image (see Figure S4c in the Supporting Information). A clear electric contrast extending hundreds of nm outside the bubble is observed (green line), while this is absent in the topography (gray line) and the dielectric image (pink line). f) Simulated topography image of a triangular bubble in monolayer hBN and corresponding calculated g) electric-field energy density and h) polarization (vector field) and charge distribution (colormap). Color scales (from dark to bright): topography (both experimental and simulated) 20 nm; EFM 1.5 V; electric field energy density  $1.5 \mu\text{V } \text{\AA}^{-2}$ ; charge distribution  $-6 \times 10^{12}$  (green) to  $6 \times 10^{12}$  (pink)  $\text{e}^{-} \text{cm}^{-2}$ .

the bubble are flat and featureless (see profile in Figure 1e), except for the creases from which the bubble originates. In contrast, the electric image (Figure 1d) clearly shows bright areas surrounding the bubble which are not found in the dielectric image (see Figure S4c in the Supporting Information), as evidenced by the corresponding profiles (Figure 1e). We therefore conclude that such localized electric-field variations around the bubbles originate from the hBN being strongly strained in these areas. Additional images of triangular and elliptical bubbles further support this interpretation (see Figures S4d–f and S5, respectively, in the Supporting Information).

To support our experimental observations, we theoretically calculated the piezoelectric behavior of monolayer hBN in the presence of bubbles and creases that mimic those experimentally observed. Figure 1f–h plots the results of our simulations for the case of a triangular bubble similar to that experimentally observed in Figure 1c,d. The shape of the bubble is given by the equilibrium configuration of material trapped between a flat substrate and a 2D crystal attracted by van der Waals forces, as described in ref. [4]. For this shape, we solved the discretized elasticity equations for the membrane with a honeycomb lattice (see the Experimental Section and Sections S3 and S4 in the Supporting Information), thus providing the strain tensor  $u_{jk}$  and hence the piezoelectric induced polarization  $P_i(\mathbf{r}) = \sum_{jk} \gamma_{ijk} u_{jk}(\mathbf{r})$ , being  $\gamma_{ijk}$  the 3rd rank piezoelectric tensor. For 2D crystals with  $D_{3h}$  symmetry lying in the  $xy$ -plane (we choose the  $x$ -direction parallel to the zigzag edge, and the  $y$ -direction parallel to the armchair edge), the only nonzero-independent coefficient is<sup>[5]</sup>  $\gamma \equiv \gamma_{yyy} = -\gamma_{yxx} = -\gamma_{xyx} = -\gamma_{xxy}$ . For the case of hBN and related 2D crystals with hexagonal symmetry, the polarization can be written as<sup>[5,13]</sup>  $\mathbf{P}(\mathbf{r}) = \gamma \mathcal{A}(\mathbf{r}) \times \hat{\mathbf{z}}$ , where  $\mathcal{A}(\mathbf{r}) = (u_{xx}(\mathbf{r}) - u_{yy}(\mathbf{r})) \hat{\mathbf{x}} - 2u_{xy}(\mathbf{r}) \hat{\mathbf{y}}$  has the form of the gauge field that appears in strained graphene.<sup>[14]</sup> We used the modern theory of polarization that exploits the geometrical properties of the Bloch wave-functions to obtain the electronic polarization,<sup>[15]</sup> a method that has been applied to noncentrosymmetric hexagonal nanotubes<sup>[16]</sup> and 2D crystals.<sup>[5,13]</sup> In particular, it has been shown that it is possible to express the piezoelectric coefficient in terms of the valley Chern number.<sup>[5]</sup> For the case of interest here, the piezoelectric coefficient of hBN takes the simple form  $\gamma = \eta \frac{e}{4\pi a_0} C_{\text{valley}} \approx 2.91 \times 10^{-10} \text{ Cm}^{-1}$ , where  $\eta \approx 3.3$  is the electron-phonon coupling in hBN,<sup>[13]</sup>  $a_0 = 1.44 \text{ \AA}$  is the interatomic distance,  $e$  is the elementary charge, and  $C_{\text{valley}} = \sum_{\tau} \tau C_{\tau} = \text{sign}(\Delta)$  is the valley Chern number, where  $\tau$  is the valley index,  $\Delta \approx 5.97 \text{ eV}$  is the hBN bandgap, and  $C_{\tau} = \tau \text{sign}(\Delta)/2$ . We refer to Experimental Section and Supporting Information for details in the numerical simulations steps. From these calculations, we obtained the energy density generated by the piezoelectric effect (Figure 1g), and the spatial distribution of the electronic polarization  $\mathbf{P}(\mathbf{r})$  and the piezoelectric charge density  $\rho(\mathbf{r})$  (Figure 1h). Our simulations predict high contrast in energy density in the strained areas around the bubbles in correspondence of piezoelectric charge densities, in good agreement with our observations (Figure 1d). This can be understood as the EFM electric signal detects the electric field variations arising from local charge densities.<sup>[10a,c]</sup> Our simulations predict a minimum in the center of the bubbles, which we experimentally detected in some of the EFM electric images (Figure 1b). However, the EFM contrast over the bubbles is affected by other important

contributions in addition to piezoelectricity, including the dielectric properties of the molecules trapped inside, as already mentioned above, possible doping effects arising from them, and topographic artifacts. Therefore, we limited our analysis to the experimental contrast observed outside the bubbles, where atomically flat and clean interfaces are present as a result of the self-cleansing mechanism of hBN crystals which pushes contamination away from the interfaces and gathers it into bubbles.<sup>[17]</sup> We theoretically analyzed the triangular bubble at different orientations with respect to the crystallographic axes (see Figure S15 in the Supporting Information). We found that the energy density distribution does not depend on the bubble orientation, which is also consistent with our experimental observations. We note that a slight anisotropy in the contrast was experimentally detected around some bubbles. We attribute it to the asymmetries and imperfections of real bubbles as compared to the perfectly symmetric shapes of the bubbles that we simulated as well as to the asymmetric shape and scan angle of the AFM probe used in the experiments.

To better understand the experimental results, we investigated their dependence on the bottom layer used in our experiments. To this aim, we fabricated and measured heterostructures in which the monolayer hBN was transferred on a graphene layer instead of hBN crystals. Figure 2 plots representative experimental results for monolayer hBN on top of graphene. As shown in the topography image (Figure 2a), we found bubbles and creases with size and shape similar to those observed on hBN crystals. The corresponding EFM electric image (Figure 2b) also shows bright contrast in many flat areas extending hundreds of nanometers around and between bubbles and creases, as in the case of using hBN crystals as bottom layer. This contrast again vanishes in the corresponding dielectric image (see Figure S6c in the Supporting Information), showing no features around or between bubbles. Images obtained in other regions confirm these observations (see Figure S6d–f in the Supporting Information). Again, we did not observe any bright feature in the electric images in the absence of bubbles and creases (see Figure S7 in the Supporting Information). We thus conclude that the local electric variations observed in our experiments do not originate in the bottom layer. They are the consequence of the strain in the hBN monolayer around bubbles and creases, in agreement with our theoretical analysis. As a further evidence, we found that for monolayer hBN on graphene, such bright areas tend to extend over larger regions and have higher directionality than those found on hBN crystals (see also Supporting Information). Figure 2d is a close-up electric image in one of these regions between two bubbles in monolayer hBN on graphene. The corresponding topography image (Figure 2c) reveals the presence of atomically thin creases (height  $\approx 3 \text{ \AA}$ ) connecting the two bubbles. Figure 2e shows a high-resolution topographic image of a region around another bubble where atomically thin creases are clearly visible. These ultrathin creases, which are associated with strain concentration and release around the bubbles,<sup>[4,18]</sup> produce additional strain and, therefore, generate an electric field that concentrates between bubbles. To support this conclusion, we simulated the case of two elliptical bubbles in the presence of atomically thin creases (Figure 2f–h), which mimic the ones observed in Figure 2c (see also Figure S17,

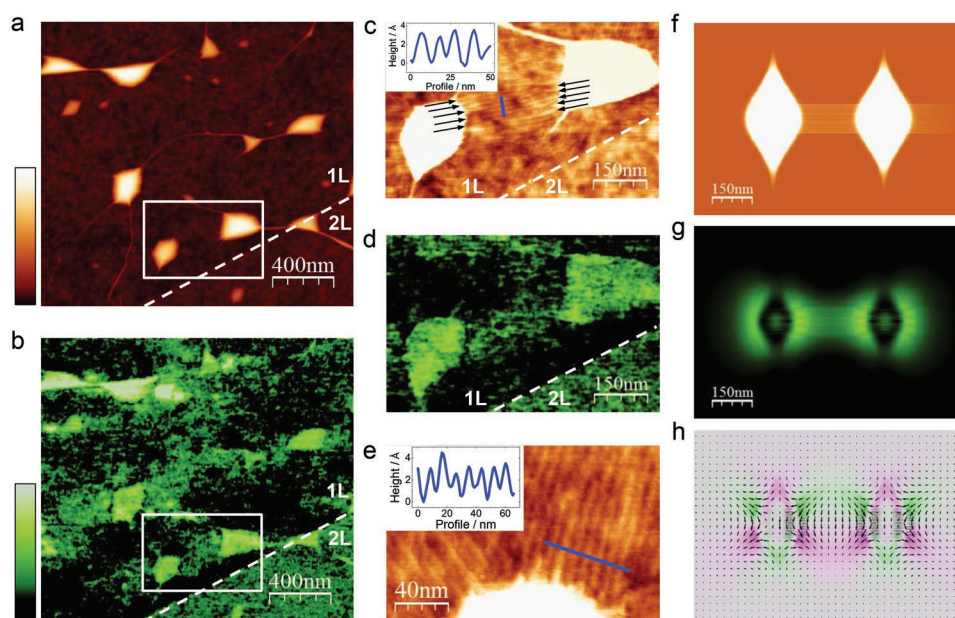


**Figure 2.** Monolayer hBN on graphene. a) Topography of a representative region with bubbles and creases. The dashed line separates a monolayer area (main part of the image) from a bilayer terrace (bottom right corner). b) Corresponding EFM electric image, showing enhanced contrast around and between bubbles in the monolayer. c) Zoom-in on the region indicated by the rectangle in (a) showing atomically thin creases (marked by black arrows) between two bubbles. The inset is the topography profile taken along the blue line. d) Corresponding electric image, showing enhanced contrast in correspondence of such ultrathin creases. e) High-resolution topography image close to another bubble where ultrathin creases are clearly visible. The inset is the topography profile taken along the blue line. f) Simulated topography of two elliptical bubbles connected by atomically thin creases and corresponding calculated g) electric-field energy density, and h) polarization (vector field) and charge distribution (colormap). Color scales (from dark to bright): topography 20 nm in (a), 2 nm in the rest; EFM 1.5 V; electric field energy density  $75 \mu\text{V } \text{\AA}^{-2}$ ; charge distribution  $-6 \times 10^{12}$  (green) to  $6 \times 10^{12}$  (pink)  $\text{e}^- \text{cm}^{-2}$ . The height of the bubbles in (c), (e), (f) was 20 nm, the color scale in these panels was adjusted to 2 nm to visualize the atomically thin creases.

Supporting Information). The calculated electric field energy density image (Figure 2g) clearly exhibits higher contrast that extends between the two bubbles and matches the bright contrast observed in the EFM image in Figure 2d.

To further support our experimental results, we fabricated and measured a series of control heterostructures for which no piezoelectricity is expected. In particular, we investigated the case of bilayer hBN, where the center of symmetry is restored, as well as the case of graphene, which is centrosymmetric because of the presence of the same element in the two sublattices of its unit cell. **Figure 3** shows representative topography and EFM electric images of three heterostructures: bilayer hBN on thick hBN crystals, bilayer hBN on graphene, and graphene on graphene. Images were taken under the same experimental conditions as in Figures 2 and 3. In all the cases, we found bubbles of similar size and shape as those found in monolayer hBN (Figure 3a,c,e). The EFM electric images (Figure 3b,d,f) showed the usual high contrast over the bubbles due to the presence of trapped molecules, but no features outside the bubbles, in contrast with our observations in monolayer hBN (also see the dielectric images in Figure S8 in the Supporting Information). We consistently found this behavior for all the bubbles in bilayer hBN irrespective of the bottom layer as well as in graphene on graphene. Figures S9 and S10 in the Supporting Information report additional images of different areas and bubbles in the control heterostructures. Furthermore, Figure S11 in the Supporting Information shows AFM and EFM images of few-layer hBN on both thick hBN crystals

and graphene layers, in which we did not observe any sign of electric contrast outside the bubbles. All these experimental observations agree with the expected absence of piezoelectricity in bilayer and bulk hBN as well as in graphene. This strongly supports our interpretation of the electric contrast found in monolayer hBN as evidence of piezoelectricity. This also proves that other possible sources of contrast such as doping effects arising from the underlying layer, the presence of adsorbates or free carriers, which are not included in our simulations, are negligible, otherwise we would have detected them in these control measurements. Finally, we note that we found the presence of atomically thin creases around the bubbles in graphene over graphene (Figure S10d in the Supporting Information) similarly as in monolayer hBN on graphene. However, no contrast was observed in the corresponding electric images. This clearly rules out that the strain-induced electric field detected in monolayer hBN in the presence of such ultrathin creases (Figure 2d) originates in the underlying graphene. It again supports our interpretation of such contrast as sign of piezoelectricity in the monolayer hBN.

In summary, the experimental evidence that we have presented here clearly indicates the generation of piezoelectric fields in highly strained monolayer hBN. We directly visualized the local electric field generated in the monolayer by strained regions around bubbles and creases, irrespective of the underlying substrate, while this is absent in bilayer hBN, few-layer hBN, and graphene, in agreement with the theory. We calculated the piezoelectric coefficient of hBN, obtaining

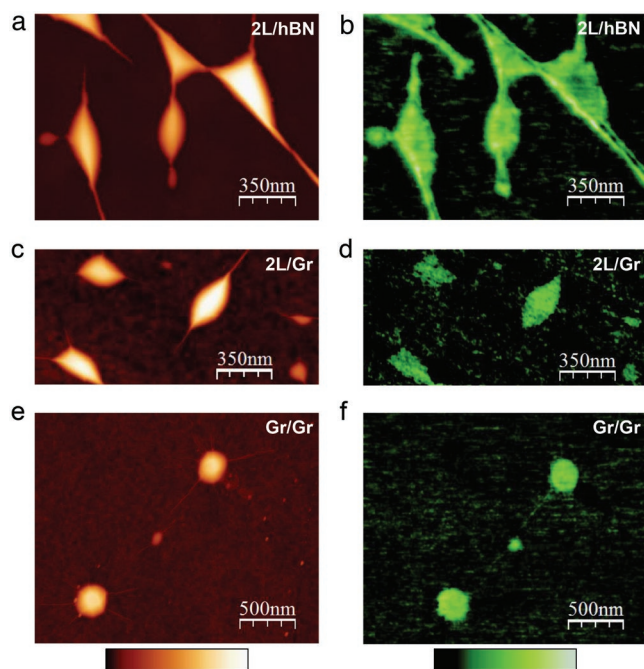


**Figure 3.** Control heterostructures: top) bilayer hBN on thick hBN crystal, middle) bilayer hBN on graphene; and lower) graphene on graphene. a,c,e) Topography of representative regions with bubbles and creases and b,d,f) corresponding electric images (see corresponding dielectric images in Figure S8 in the Supporting Information). Contrary to the case of monolayer hBN (Figures 1 and 2), no bright areas were detected around or between bubbles in the electric images. Color scales (from dark to bright): topography 20 nm; EFM 1.5 V.

$\gamma \approx 2.91 \times 10^{-10} \text{ Cm}^{-1}$  ( $0.9 \text{ Cm}^{-2}$  when normalized by the layer thickness). This value is comparable to the bulk values of conventional piezoelectric materials such as ZnO, AlN, and lead zirconate titanate (PZT) ceramics.<sup>[19]</sup> We can estimate the induced polarization and the electric field energy density due to the anisotropic strain gradient in our monolayer hBN membranes. Although they vary strongly, they can reach relatively high levels in some regions,  $\approx 10^{12} \text{ e}^- \text{ cm}^{-2}$  and  $\approx 10^{-6} \text{ eV } \text{ \AA}^{-2}$ , respectively. These are comparable to the carrier concentration in doped graphene<sup>[20]</sup> and to the energy density in capacitors used in microelectronic circuits<sup>[21]</sup> if scaled to two-dimensionality. Such strain-induced electric fields can provide a significant scattering mechanism if monolayer hBN is used as encapsulation layer on top of graphene. At the same time, one can envisage that special distribution of the carrier density in graphene can be altered via strain in such monolayer encapsulation layer. Alternative methods to engineer the local strain could be used, such as the use of periodic arrays of nanopillars,<sup>[22]</sup> and locally control the electric fields. The piezoelectricity of single-layer hBN opens the door to its combination with other 2D crystals for the development of devices with novel functionalities and self-powering potential. These results are also important as they show that electrostatic scanning probe techniques such as EFM used here or Kelvin probe force microscopy (which simply employs an additional feedback to detect electric variations at the first harmonic,  $\omega$ ) are able to detect piezoelectricity of materials on the nanoscale.

## Experimental Section

**Samples Preparation:** Samples were fabricated using the standard dry transfer technique. Briefly, monolayer hBN was mechanically exfoliated and identified on a double-polymer layer of polymethylglutaramide (PMGI) and poly(methyl methacrylate) (PMMA). The PMGI layer was developed from beneath the PMMA layer to create a free-standing and easily manipulated membrane with the crystal on top. The membrane was then inverted and positioned above the bottom layer (thick hBN or graphene) using a set of micromanipulation stages—with accuracy better than 5  $\mu\text{m}$ . The crystals were then brought into contact. The PMMA was removed by simply peeling back the membrane, meaning no solvent come into contact with either crystal to preserve the cleanliness of the top surface.

**AFM and EFM Imaging:** Simultaneous AFM and EFM images were acquired using a Nanotec Electronica AFM (see Supporting Information Section S1 for details). The EFM force gradient was measured at the first and second harmonic by using a phase-lock loop and a multi-frequency lock-in amplifier (Zurich Instruments). n-Doped silicon probes were used (Nanosensors PPP-FMR and PPP-XYNCSTR, mechanical resonance frequencies  $\approx 65$  and 137 kHz and spring constants  $\approx 1.8$  and  $5.3 \text{ Nm}^{-1}$ , respectively), calibrated using the Sader's method.<sup>[23]</sup> Doped silicon tips had the advantage of a tip radius of only a few nanometers, one order of magnitude smaller than the typical radius of metal-coated probes, thus increasing the lateral resolution of both topography and EFM images. Furthermore, unlike metal-coated probes, n-doped silicon probes suffered no substantial tip modifications during imaging and, therefore, ensured stable measurement conditions.<sup>[24]</sup> The cantilever was oscillated in resonance with free amplitudes below 20 nm and setpoints imposing minimum amplitude reduction. The cantilever was excited with an AC voltage of amplitude 4–6 V and frequency 1.8 kHz. These measurement conditions were carefully chosen to minimize all possible sources of cross-talk.<sup>[25]</sup> The data were acquired and processed using WSxM software.<sup>[26]</sup> All EFM images in this work were presented with the same scale, contrast, and offset for better comparison.

**Theoretical Calculations:** For a given strain profile, the induced charge density was obtained from the local variation of the polarization as  $\rho(\mathbf{r}) = e n(\mathbf{r}) = -\nabla \cdot \mathbf{P}(\mathbf{r}) = -\gamma \hat{z} \cdot [\nabla \times \mathcal{A}(\mathbf{r})]$ . The numerical calculation involved the following steps (see Supporting Information Sections S3 and S4 for details): i) The equilibrium configuration of a deformed single-layer hBN membrane (61 200 or 242 000 atoms, depending on the cases, clamped boundary conditions) was obtained from the numerical solution of the discretized elasticity equations for a given shape (e.g., circular, triangular, or elliptical bubbles). ii) The solution gave the strain fields  $u_{ij}(\mathbf{r})$  generated in the crystal that minimize the energy, which entered in the vector potential  $\mathcal{A}(\mathbf{r})$  and which was used to calculate the spatial distribution of electronic polarization  $\mathbf{P}(\mathbf{r})$ , piezoelectric charge density  $\rho(\mathbf{r})$ , the energy density generated by the piezoelectric effect  $u_E(\mathbf{r}) = |\mathbf{P}(\mathbf{r})|^2 / (2\epsilon_{2d})$ , where  $\epsilon_{2d}$  is the dielectric constant of the hBN film.

## Supporting Information

Supporting Information is available from the Wiley Online Library or from the author.

## Acknowledgements

The authors acknowledge support from EU Graphene Flagship Program (contract CNECTICT-604391), European Research Council Synergy Grant Hetero2D, the Royal Society, Engineering and Physical Sciences Research Council (UK, grant number EP/N010345/1), US Army Research Office (W911NF-16-1-0279). P.A. and L.F. received funding from the EU Research and Innovation Program under the Marie Skłodowska-Curie grant agreement no. 793394.

## Conflict of Interest

The authors declare no conflict of interest.

## Keywords

2D materials, electrostatic force microscopy, hexagonal boron nitride, piezoelectricity

Received: August 24, 2019

Revised: October 18, 2019

Published online: November 18, 2019

- [1] C. Brown, R. Kell, R. Taylor, L. Thomas, *IRE Trans. Compon. Parts* **1962**, 9, 193.
- [2] a) A. Falin, Q. R. Cai, E. J. G. Santos, D. Scullion, D. Qian, R. Zhang, Z. Yang, S. M. Huang, K. Watanabe, T. Taniguchi, M. R. Barnett, Y. Chen, R. S. Ruoff, L. H. Li, *Nat. Commun.* **2017**, 8, 15815; b) C. Lee, X. D. Wei, J. W. Kysar, J. Hone, *Science* **2008**, 321, 385.
- [3] a) W. Z. Wu, L. Wang, Y. L. Li, F. Zhang, L. Lin, S. M. Niu, D. Chenet, X. Zhang, Y. F. Hao, T. F. Heinz, J. Hone, Z. L. Wang, *Nature* **2014**, 514, 470; b) H. Y. Zhu, Y. Wang, J. Xiao, M. Liu, S. M. Xiong, Z. J. Wong, Z. L. Ye, Y. Ye, X. B. Yin, X. Zhang, *Nat. Nanotechnol.* **2015**, 10, 151.
- [4] E. Khestanova, F. Guinea, L. Fumagalli, A. K. Geim, I. V. Grigorieva, *Nat. Commun.* **2016**, 7, 12587.
- [5] H. Rostami, F. Guinea, M. Polini, R. Roldán, *npj 2D Mater. Appl.* **2018**, 2, 15.
- [6] a) L. H. Li, J. Cervenka, K. Watanabe, T. Taniguchi, Y. Chen, *ACS Nano* **2014**, 8, 1457; b) L. H. Li, Y. Chen, *Adv. Funct. Mater.* **2016**, 26, 2594; c) L. H. Li, Y. Chen, B. M. Cheng, M. Y. Lin, S. L. Chou, Y. C. Peng, *Appl. Phys. Lett.* **2012**, 100, 261108; d) T. T. Tran, K. Bray, M. J. Ford, M. Toth, I. Aharonovich, *Nat. Nanotechnol.* **2016**, 11, 37.
- [7] C. R. Dean, A. F. Young, I. Meric, C. Lee, L. Wang, S. Sorgenfrei, K. Watanabe, T. Taniguchi, P. Kim, K. L. Shepard, J. Hone, *Nat. Nanotechnol.* **2010**, 5, 722.
- [8] K. A. N. Duerloo, M. T. Ong, E. J. Reed, *J. Phys. Chem. Lett.* **2012**, 3, 2871.
- [9] a) Y. Martin, D. W. Abraham, H. K. Wickramasinghe, *Appl. Phys. Lett.* **1988**, 52, 1103; b) J. E. Stern, B. D. Terris, H. J. Mamin, D. Rugar, *Appl. Phys. Lett.* **1988**, 53, 2717.
- [10] a) O. Cherniavskaya, L. W. Chen, V. Weng, L. Yuditsky, L. E. Brus, *J. Phys. Chem. B* **2003**, 107, 1525; b) L. Fumagalli, D. Esteban-Ferrer, A. Cuervo, J. L. Carrascosa, G. Gomila, *Nat. Mater.* **2012**, 11, 808; c) B. D. Terris, J. E. Stern, D. Rugar, H. J. Mamin, *Phys. Rev. Lett.* **1989**, 63, 2669.
- [11] L. Collins, J. I. Kilpatrick, S. A. L. Weber, A. Tselev, I. V. Vlassiouk, I. N. Ivanov, S. Jesse, S. V. Kalinin, B. J. Rodriguez, *Nanotechnology* **2013**, 24, 475702.
- [12] A. V. Kretinin, Y. Cao, J. S. Tu, G. L. Yu, R. Jalil, K. S. Novoselov, S. J. Haigh, A. Gholinia, A. Mishchenko, M. Lozada, T. Georgiou, C. R. Woods, F. Withers, P. Blake, G. Eda, A. Wirsig, C. Hucho, K. Watanabe, T. Taniguchi, A. K. Geim, R. V. Gorbachev, *Nano Lett.* **2014**, 14, 3270.
- [13] M. Droth, G. Burkard, V. M. Pereira, *Phys. Rev. B* **2016**, 94, 075404.
- [14] F. Guinea, M. I. Katsnelson, A. K. Geim, *Nat. Phys.* **2010**, 6, 30.
- [15] R. Resta, *Rev. Mod. Phys.* **1994**, 66, 899.
- [16] E. J. Mele, P. Kral, *Phys. Rev. Lett.* **2002**, 88, 056803.
- [17] K. S. Novoselov, A. Mishchenko, A. Carvalho, A. H. C. Neto, *Science* **2016**, 353, aac9439.
- [18] N. Bowden, S. Brittain, A. G. Evans, J. W. Hutchinson, G. M. Whitesides, *Nature* **1998**, 393, 146.
- [19] a) L. Bellaiche, D. Vanderbilt, *Phys. Rev. Lett.* **1999**, 83, 1347; b) H. Momida, T. Oguchi, *Appl. Phys. Express* **2018**, 11, 041201.
- [20] S. Pisana, M. Lazzeri, C. Casiraghi, K. S. Novoselov, A. K. Geim, A. C. Ferrari, F. Mauri, *Nat. Mater.* **2007**, 6, 198.
- [21] D. H. Choi, C. Randall, E. Furman, B. H. Ma, U. B. Balachandran, S. H. Zhang, M. Lanagan, in *IEEE Int. Workshop on Integrated Power Packaging*, IEEE, Piscataway, NJ, USA **2015**, p. 52.
- [22] a) Y. Jiang, J. Mao, J. Duan, X. Lai, K. Watanabe, T. Taniguchi, E. Y. Andrei, *Nano Lett.* **2017**, 17, 2839; b) A. Reserbat-Plantey, D. Kalita, Z. Han, L. Ferlazzo, S. Autier-Laurent, K. Komatsu, C. Li, R. Weil, A. Ralko, L. Marty, S. Gueron, N. Bendiab, H. Bouchiat, V. Bouchiat, *Nano Lett.* **2014**, 14, 5044.
- [23] J. E. Sader, J. W. M. Chon, P. Mulvaney, *Rev. Sci. Instrum.* **1999**, 70, 3967.
- [24] a) A. Gil, J. Colchero, J. Gómez-Herrero, A. M. Baró, *Nanotechnology* **2003**, 14, 332; b) T. Glatzel, S. Sadewasser, M. C. Lux-Steiner, *Appl. Surf. Sci.* **2003**, 210, 84; c) S. Kitamura, M. Iwatsuki, *Appl. Phys. Lett.* **1998**, 72, 3154.
- [25] L. Collins, Y. Liu, O. S. Ovchinnikova, R. Proksch, *ACS Nano* **2019**, 13, 8055.
- [26] a) A. Gimeno, P. Ares, I. Horcas, A. Gil, J. M. Gomez-Rodriguez, J. Colchero, J. Gomez-Herrero, *Bioinformatics* **2015**, 31, 2918; b) I. Horcas, R. Fernandez, J. M. Gomez-Rodriguez, J. Colchero, J. Gomez-Herrero, A. M. Baro, *Rev. Sci. Instrum.* **2007**, 78, 013705.